8-2016

Relative Sensitivities of DCE-MRI Pharmacokinetic Parameters to Arterial Input Function (AIF) Scaling

Xin Li
Oregon Health & Science University

Yu Cai
Oregon Health & Science University

Brendan Moloney
Oregon Health & Science University

Yiyi Chen
Oregon Health & Science University

Wei Huang
Oregon Health & Science University

See next page for additional authors

Citation Details

Published as: Li, X., Cai, Y., Moloney, B., Chen, Y., Huang, W., Woods, M., … Springer, C. S., Jr (2016). Relative sensitivities of DCE-MRI pharmacokinetic parameters to arterial input function (AIF) scaling. Journal of magnetic resonance (San Diego, Calif. : 1997), 269, 104–112. doi:10.1016/j.jmr.2016.05.018

HHS Public Access

Author manuscript

J Magn Reson. Author manuscript; available in PMC 2017 August 01.

Published in final edited form as:

J Magn Reson. 2016 August ; 269: 104–112. doi:10.1016/j.jmr.2016.05.018.

Relative sensitivities of DCE-MRI pharmacokinetic parameters to arterial input function (AIF) scaling

Xin Li[1], **Yu Cai**[1], **Brendan Moloney**[1], **Yiyi Chen**[2], **Wei Huang**[1], **Mark Woods**[1], **Fergus V. Coakley**[3], **William D. Rooney**[1], **Mark G. Garzotto**[4,5], and **Charles S. Springer Jr**[1]

[1]Advanced Imaging Research Center, Oregon Health & Science University, Portland, OR 97239

[2]Division of Biostatistics, Dept. of Public Health and Preventive Medicine, Knight Cancer Institute, Oregon Health and Science University, Portland, OR 97239

[3]Department of Diagnostic Radiology, Oregon Health & Science University, Portland, OR 97239

[4]Department of Urology, Oregon Health & Science University, Portland, OR 97239

[5]Portland VA Medical Center, Portland, OR 97239

Abstract

Dynamic-Contrast-Enhanced Magnetic Resonance Imaging (DCE-MRI) has been used widely for clinical applications. Pharmacokinetic modeling of DCE-MRI data that extracts quantitative contrast reagent/tissue-specific model parameters is the most investigated method. One of the primary challenges in pharmacokinetic analysis of DCE-MRI data is accurate and reliable measurement of the arterial input function (AIF), which is the driving force behind all pharmacokinetics. Because of effects such as inflow and partial volume averaging, AIF measured from individual arteries sometimes require amplitude scaling for better representation of the blood contrast reagent (CR) concentration time-courses. Empirical approaches like blinded AIF estimation or reference tissue AIF derivation can be useful and practical, especially when there is no clearly visible blood vessel within the imaging field-of-view (FOV). Similarly, these approaches generally also require magnitude scaling of the derived AIF time-courses. Since the AIF varies among individuals even with the same CR injection protocol and the perfect scaling factor for reconstructing the ground truth AIF often remains unknown, variations in estimated pharmacokinetic parameters due to varying AIF scaling factors are of special interest. In this work, using simulated and real prostate cancer DCE-MRI data, we examined parameter variations associated with AIF scaling. Our results show that, for both the fast-exchange-limit (FXL) Tofts model and the water exchange sensitized fast-exchange-regime (FXR) model, the commonly fitted CR transfer constant (K^{trans}) and the extravascular, extracellular volume fraction (v_e) scale nearly proportionally with the AIF, whereas the FXR-specific unidirectional cellular water efflux rate constant, k_{io}, and the CR intravasation rate constant, k_{ep}, are both AIF scaling insensitive. This

Corresponding author: Xin Li, Advanced Imaging Research Center, Oregon Health & Science University, Portland, OR 97239, Tel: 503-418-1533, Fax: 503-418-1543, lxin@ohsu.edu.

indicates that, for DCE-MRI of prostate cancer and possibly other cancers, k_{io} and k_{ep} may be more suitable imaging biomarkers for cross-platform, multicenter applications. Data from our limited study cohort show that k_{io} correlates with Gleason scores, suggesting that it may be a useful biomarker for prostate cancer disease progression monitoring.

Graphical abstract

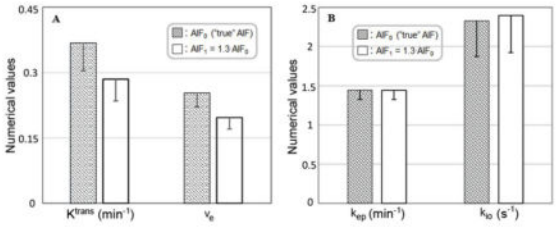

Keywords

Dynamic-Contrast-Enhanced; water exchange; arterial input function; contrast reagent; AIF scaling; prostate cancer

INTRODUCTION

Dynamic-contrast-enhanced MRI [DCE-MRI] is widely used in the study of cancer and other pathologies. It provides high-resolution anatomical [lesion size, shape], microvascular [tumor blood volume, capillary permeability] [1–6] and, potentially metabolic [Na^+,K^+ ATPase activity] information [7,8]. The quantitative estimation of DCE-MRI pharmacokinetic parameters requires knowledge of the time-dependences of the plasma and interstitial compartmental contrast reagent (CR) concentrations, $[CR_p](t)$ and $[CR_o](t)$, respectively. The former is commonly referred to as the arterial input function [AIF]. In practice, direct determination of either concentration time-course is not straightforward. Classical methods using radiotracer-labeled CR require frequent blood sampling for $[CR_p](t)$ and sacrificial autoradiography for $[CR_o](t)$ determinations [9,10]. These make them cumbersome and impossible, respectively, for human studies. Furthermore, blood sampling is usually from a large vessel, not a capillary adjacent to the tissue of interest, and autoradiographic estimation of the tissue interstitial distribution volume has considerable systematic uncertainty.

Thus, the common practice is to estimate $[CR_p](t)$ and $[CR_o](t)$ noninvasively, from the DCE-MRI data themselves. However, the accuracy of AIF derived from DCE-MRI data can be influenced by several inherent experimental conditions, such as: 1) partial volume effect (signal from the image voxel, ideally containing only blood, is contaminated with signal from other non-blood tissues); 2) in-flow effect (signals generated by water molecules in the blood that were originally outside of the imaging volume flow in during signal acquisition and impact the final “blood” signal detected); 3) flow-profile dependency (when vessel cross-section contains more than one image voxel, measured voxel blood CR concentration is flow-profile dependent); and 4) no visible vessel in the imaging field-of-view (FOV).

These factors can cause errors in the AIF amplitudes computed directly from blood vessel signals, and a scaling factor may be applied to reduce the errors [5,6]. Alternative methods mitigating the challenges of AIF quantification from blood signal have been proposed. Examples of these include reference tissue methods [11–13] and blinded AIF estimation [14–16]. Unfortunately, these approaches also require AIF amplitude scaling after derivation of the AIF time-course curves. The scaling factor (β) is often derived from literature reported tissue properties and generally does not account for individual variations. The AIF scaling uncertainties propagate to errors in the derived DCE-MRI pharmacokinetic modeling parameters. Thus, it is important to understand the effect of AIF scaling variations on modeled parameter values.

In this work, simulated DCE-MRI time-courses based on prostate data were subjected to repeated model fittings with the β of an AIF being the only variable. Repeated fittings of actual prostate region-of-interest (ROI) data were also performed to confirm the simulation findings. We used both the standard Tofts model and the Shutter-Speed model for data fitting. The former ignores intercompartmental water exchange (equivalent to assuming infinitely fast water exchange kinetics [the fast-exchange-limit (FXL)] pertains throughout the CR time-course), while the latter accounts for the effects of intercompartmental water exchange. The FXR (fast-exchange-regime) version of the Shutter-Speed Paradigm (SSP) was used in this study with the parameter k_{io} (unidirectional equilibrium cellular water efflux rate constant) accounting for transcytolemmal water exchange. Both models return the K^{trans} (rate constant for plasma/interstitium contrast agent transfer) and v_e (extravascular, extracellular volume fraction) parameters. When comparing all results with the common practice (β=1.0; *i.e.*, using the AIFs determined from reported methods as the reference), our results show that the commonly modeled K^{trans} and v_e values scale nearly proportionally with β, indicating that cautions should be used comparing K^{trans} and v_e values among different subjects or across different platforms. By contrast, the k_{ep} and k_{io} (SSP specific) variations are much smaller in response to the same β variations. In addition, we show that k_{io} values correlate with Gleason scores in our limited data set. This indicates that the AIF-scaling insensitive k_{io} may offer a quantitative way for prostate cancer disease aggressiveness detection or monitoring.

MATERIAL and METHODS

Prostate DCE-MRI data were acquired from 13 subjects under a study protocol approved by the Portland VA Medical Center (PVAMC) and Oregon Health & Science University (OHSU) institutional review boards (IRBs). Each subject was referred for biopsy as standard care and volunteered for our DCE-MRI protocol before that procedure occurred. A prior biopsy was an exclusion criterion. All participants gave written informed consent. Additional details are reported in [5,6].

MRI

All prostate MRI data were acquired with a Siemens TIM Trio (3T) system. RF transmission utilized the instrument whole body coil, while reception employed a combination of flexible body and spine matrix coil arrays. Multi-slice T_2-weighted images (Turbo Spin Echo,

TR/TE/FA, 5000 ms/102 ms/90°) were acquired for anatomic contrast and ROI selection [a 320*180*16 matrix size and 360*360 mm^2 transverse FOV resulted in nominal $(1.1)^2$ mm^2 in-plane resolution: slice thickness, 3 or 3.2 mm]. A near proton density (PD) image of the prostate gland was obtained using a 3D fast low-angle shot (FLASH) pulse sequence with a 256*144*16 matrix size and a 360*203 mm^2 transverse FOV, resulting in a nominal in-plane resolution of $(1.4)^2$ mm^2. Other parameters were: slice thickness, 3 or 3.2 mm; TR/TE/FA, 200 ms/1.56 ms/8°. For DCE-MRI, the same FLASH sequence was run with the only differences being TR = 5.0 ms and a 15° flip angle, which yielded a 6.28 s imaging inter-sampling interval. The total DCE-MRI acquisition time was ten and a half minutes. A bolus of 0.1 mmol/kg Prohance (Bracco, Inc.) was administered in an antecubital vein ~ 38 s after commencing the DCE-MRI acquisition. It was delivered in 5 to 10 s, at 3.0 mL/s, followed by a 20 mL saline flush.

Prostate Biopsy and Pathology

Subsequent to the DCE-MRI acquisition, each subject underwent a standard ten core "geographic" prostate biopsy procedure performed using (exclusively) ultrasound guidance; *i.e.*, with no MRI input. Pathology examinations of biopsy core specimen fragments revealed Gleason scores ranging from 6 to 8 for five of the subjects. No malignancy was found for the other eight subjects.

Data Preparation

For DCE-MRI analysis, one ROI was selected for each of the 13 subjects [6] resulting in five malignant and eight benign ROI DCE-MRI time-courses. Since the precise biopsy track positions were not recorded, the spatial relationships between the DCE-MRI ROIs and the biopsy *loci* were restricted to only unilaterality. The experimental AIF was determined from voxels within a femoral artery visible in the FOV [6]. An individual AIF time-course was measureable for each subject except one, due to severe motion during the DCE acquisition in the latter case. A population-averaged AIF, based on the individual AIFs from six other subjects, was used for that individual.

Pharmacokinetic Analyses

In DCE-MRI, $\Delta R_{1t}(t)$ describes the time-course of the ΔR_{1t} [$\equiv R_{1t}(t) - R_{1t}(0)$] value during the bolus CR passage; where $R_{1t}(t)$ is the measured tissue ^1H_2O longitudinal relaxation rate constant time-course and $R_{1t}(0)$ denotes the value prior to CR administration. Individual $R_{1t}(0)$ values were calculated numerically with the Gradient Recalled Echo (GRE) signal expression (Eq. 7) using the average of DCE baseline images and that of the near PD-weighted image. With $R_{1t}(0)$ determined, the $R_{1t}(t)$ time-course can be calculated from the DCE-MRI signal time-course using the signal mean from DCE baseline for PD computation. To enhance the k_{io} detection capability, especially for the fast wash-out malignant lesion cases, only the first 70 time points (7.3 min total) were included in the model fitting for the prostate data. One critical step in quantitative DCE-MRI data analysis is to relate the measured $\Delta R_{1t}(t)$ time-course to the time-course of the interstitial CR concentration time-course, $[CR_o](t)$.

The Shutter-Speed Paradigm—Because most water is inside cells but the CR visits at most the interstitial space, the kinetics of the equilibrium exchange of water molecules across the cell membranes must be taken into account. In this study we used the fast-exchange-regime (FXR)-allowed shutter-speed paradigm model that takes into account this exchange but assumes a single exponential recovery for the ^1H_2O signal [5,17,18]. This is expressed in

$$R_{1t}(t)=\frac{1}{2}\left[R_{1i}+r_{1o}[CR_o](t)+R_{1o0}+k_{io}+\frac{k_{io}v_i}{v_e}\right]-\frac{1}{2}\left\{\left[R_{1i}-r_{1o}[CR_o](t)-R_{1o0}+k_{io}-\frac{k_{io}v_i}{v_e}\right]^2+\frac{(2k_{io})^2v_i}{v_e}\right\}^{\frac{1}{2}} \quad (1)$$

where R_{1i} and R_{1o0} are, respectively, the longitudinal relaxation rate constants for the intra- and extracellular ^1H_2O signals (in the absence of exchange and CR); r_{1o} is the interstitial CR relaxivity; k_{io} is the unidirectional equilibrium cellular water efflux rate constant (reciprocal of the mean intracellular water lifetime, τ_i); and v_i and v_e are the respective intra- and extracellular volume fractions. The absolute difference in R_1 between the extra- and intracellular space ($|R_{1o}–R_{1i}|$) is defined as the "shutter-speed", τ_1^{-1} [$\equiv \kappa_1$] [17].

Using the Kety-Schmitt pharmacokinetic rate law, the interstitial CR concentration time course, $[CR_o](t)$, is expressed by Equation (2), where K^{trans} is the CR transfer rate constant

$$[CR_o](T)=K^{trans}\cdot {v_e}^{-1}\cdot\int_0^T[CR_p](t)\cdot\exp\left(-K^{trans}\cdot {v_e}^{-1}\cdot(T-t)\right)\cdot dt \quad (2)$$

and $[CR_p](t)$, the blood plasma [CR] time-course, is the AIF. The MRI experimentally determined AIF can be expressed as in Equation (3):

$$[CR_p](t)=\{R_{1b}(t)-R_{1b}(0)\}/\{(1-h_v)r_{1p}\} \quad (3)$$

where $R_{1b}(t)$ is the capillary blood ^1H_2O R_1 time-course, $R_{1b}(0)$ is the pre-CR blood R_1, r_{1p} is the longitudinal relaxivity for CR in blood plasma and fixed at a literature value of 3.8 $mM^{-1}s^{-1}$ [19], and h_v (fixed at 0.45) is the microvascular hematocrit.

To systematically account for AIF amplitude scaling, we rewrite Eq. (2) to include the time-independent AIF scaling factor, β, as Equation (4):

$$[CR_o](T)=K^{trans}\cdot v_e^{-1}\cdot\int_0^T\beta\cdot[CR_p](t)\cdot\exp\left(-K^{trans}\cdot v_e^{-1}\cdot(T-t)\right)\cdot dt \quad (4)$$

where β is a time-independent scaling factor that quantifies AIF amplitude variations.

The differential form of Eq. (4) is given in Equation (5).

$$\frac{d[CR_o]}{dt}+k_{ep}[CR_o]=k_{ep}\cdot\beta\cdot[CR_p] \quad (5)$$

It is important to point out that there is no "extra" β term in any pharmacokinetic model equations. Here, the β factor is added for the purpose of simulating AIF scaling uncertainties, with β = 1.0 representing the "ground truth" AIF. The use of β makes it easier to illustrate parameter changes associated with AIF scaling. That is "$\beta\cdot[CR_p]$" is the actual AIF used in each fitting. In Eq. (5), the K^{trans}/v_e term appearing in Eq. (4) is replaced by k_{ep} according to its definition.

Standard mathematical approach to solve an inhomogeneous first-order differential equation like Eq. (5) starts with solving its associated homogenous equation (*i. e.*, Eq. (5) with the right-hand-side set to zero, or $[CR_p]$ =0). This immediately reveals that the rate constant (k_{ep}) is not impulse function ($[CR_p]$) dependent. Specific to DCE-MRI, as long as the curve shape of $[CR_p](t)$ doesn't change, then k_{ep} is independent of β. This observation is associated with the Kety-Schmitt pharmacokinetic rate law and thus applies to both the FXL and FXR models used in this study. In practice, since the AIFs are often determined numerically without an analytical expression, there might be small variations of k_{ep} following a β change.

The Tracer Paradigm—Very often in the literature the MRI CR is treated as a tracer (*i.e.*, as if it's directly detected) and, when the blood ^1H_2O contribution to the tissue signal is negligible, the tissue R_1 change, $\Delta R_{1t}(t)$, can be expressed using $[CR_o](t)$, as in Equation (6):

$$\Delta R_{1t}(t)=r_{1o}\bullet[CR_o](t)\bullet v_e \quad (6)$$

which is simpler than Eq. (1). However, Eq. (6) implies a linear $[CR_o]$-dependence of ΔR_{1t}, which is experimentally untrue [20,21]. It further implies that equilibrium transcytolemmal water exchange kinetics are effectively infinitely fast [$k_{io}\rightarrow\infty$] [21]. This is usually an incorrect over-simplification. The direct consequences of using tracer paradigm (TP) models are systematic errors in the estimated pharmacokinetic parameters such as K^{trans} [example below] and v_e [1–3,5–7]. Nevertheless, since tracer models find common use in the literature because of their relative simplicity, we also used one, the standard, fast-exchange-limit (FXL)-constrained Tofts tracer model [22], in addition to the FXR-SSP model in assessing the effects of AIF scaling uncertainty. The k_{io} parameter is unique to the SSP models and cannot be accessed by any tracer paradigm model because such models effectively assume k_{io} to approach infinity [$k_{io}\rightarrow\infty$]. Mathematically, Eq. (1) simplifies to the FXL Eq. (6) when $\kappa_1\rightarrow 0$ [21]. Thus, the SSP-FXR automatically simplifies to the Tofts FXL model if κ_1 (the shutter-speed) never rises sufficiently during a DCE time-course. However, this does not mean that $k_{io}\rightarrow\infty$, only that k_{io} is indeterminate.

Simulations

The $[CR_o]$ expression in Eq. (4) was used by both the SSP and TP approaches. For a given K^{trans}, v_e, and k_{io} (SSP only) parameter set, $R_{1t}(t)$ time courses are influenced by AIF scaling through the associated input function $\beta\cdot[CR_p]$, where $[CR_p]$ (the reference or "true" AIF when $\beta = 1.0$) used for the simulation was based on our experimental measurements and further smoothed to mimic a well-determined AIF (see Figure 1A). K^{trans}, v_e, and k_{io} values were selected based on those from the prostate data. Unless otherwise stated, we simulated R_{1t} time-courses using the conventional β =1.0. After the R_{1t} calculation, Equation (7) suitable for gradient-echo sequence was used to calculate the signal time-courses.

$$S = S_0 \frac{(1-\exp(-TR\cdot R_{1t}))}{(1-\exp(-TR\cdot R_{1t})\cdot\cos\alpha)}\cdot\sin\alpha \quad [7]$$

Here, S_0 is proportional to the equilibrium magnetization, TR is the pulse sequence repetition time, α the read pulse flip angle. Noiseless signal time-courses as well as those with added Gaussian white noise were both used to investigate parameter variations under different β values.

Simulated time-courses were fitted with different AIFs defined as $\beta\cdot[CR_p]$. Eq. (4) suggests that β interacts inversely with K^{trans} and proportionately with v_e in data fitting. To investigate parameter variations caused by different AIF scaling, simulations were carried out by fitting pharmacokinetic parameters with β fixed at 13 different values from 0.8 to 2.0 with a step-size of 0.1. A larger than 100% β variation was included for model fittings so that parameter trends in response to AIF scaling can be better observed.

Fitting the simulated time-courses yielded K^{trans}, v_e, and τ_i ($\equiv 1/k_{io}$, SSP only) values. In addition, k_{ep} [$\equiv K^{trans}/v_e$] [22], and the intracellular volume fraction v_i [$\equiv 1 - v_e$] values were determined. While v_e defines the CR accessible volume fraction, the v_i parameter equals the cell density [ρ] and mean individual cell volume (<V>) product [ρ •<V>], within the ROI or voxel [7].

To avoid local minima in each optimization procedure, 20 different initial guess parameter value sets were used for each β step and each model. Parameters from the best fitting of the 20 trials for each combination were then selected as the fitted results. In addition, two-dimensional grid searches [3,23] were also performed to investigate the K^{trans}-v_e parameter space to gain insights into the fitting approaches and to provide assurance in avoiding potential local minima during fitting.

RESULTS

Figure 1A plots the averaged blood plasma concentration, $[CR_p]$, time-course derived from five individual AIFs [6]. Under the condition of β =1.3 (*i.e.,* 130% the AIF amplitude as show in 1A), the solid curve in **1B** plots the $\Delta R_1(t)$ time-course predicted by the shutter-speed approach for k_{ep} = 1.2 min^{-1}, v_i = 0.70, and k_{io} = 1.7 s^{-1} [K^{trans} = 0.36 min^{-1}, v_e = 0.30, τ_i = 0.60s]. The 1B dashed curve shows the prediction for k_{ep} = 1.1 min^{-1}, v_i = 0.68,

and k_{io} = 1.7 s^{-1} [K^{trans} = 0.35 min^{-1}, v_e = 0.32, τ_i = 0.60 s]. As expected, the $\Delta R_1(t)$ wash-out portion is rather sensitive to an only 8% k_{ep} reduction [there is also a 3% v_i reduction]. Also as expected, the simulated $\Delta R_1(t)$ time-courses with either parameter set are lower than the 1B curves when β=1.0 (using the AIF in 1A; not shown).

To investigate K^{trans} and v_e (and thus k_{ep} and v_i) parameter sensitivity to AIF scaling, a grid search [23] rather than a non-linear data fitting was selected as the first step of data analysis. Although the former can be tedious and slow, a large searching range can often provide the global solution and avoid local minima that could trap a non-linear optimization.

For demonstration, Figure 2A shows a search of the K^{trans}, v_e error surface. Using the Fig. 1A AIF, and the parameter set of K^{trans} = 0.36 min^{-1}, v_e = 0.30, and k_{io} = 1.7 s^{-1}, the reference R_{1t} and its related reference signal time-course, $S_{ref}(t)$, were generated. Then, the simulated $R_1(t)$ for each grid point (K^{trans},v_e coordinate pair; k_{io} = 1.7 s^{-1}) and $S_{grid}(t)$ time-course was calculated and this was compared with $S_{ref}(t)$. The constant difference square sum {$\chi^2 = \Sigma t[S_{ref}(t) - S_{grid}(t)]^2$ [3]} value contours decrease to a global minimum at the coordinates K^{trans} = 0.36 min^{-1} and v_e =0.30 (k_{ep} = 1.2 min^{-1}), matching the inputs used in generating the reference curve as expected. The contour lines measure the χ^2 value ("goodness") of comparisons with the reference curve of different model curves calculated for the parameter values given by the coordinates [3]. The χ^2 value decreases as one moves on the surface towards the closed contours. Figure 2B shows the best fitted k_{ep} values determined at different β. A near constant k_{ep} [1.2 min^{-1}] is observed over the range of β tested. [Slight k_{ep} deviations are most likely due to the finite numbers of K^{trans} and v_e steps (500–600) used in the grid search.]

Using shutter-speed simulated data and analyses, Figure 3A shows K^{trans}, v_e, and τ_i changes associated with a 30% AIF scaling change. The reference parameter values (cross-hatched bars) are: K^{trans} = 0.36 min^{-1}, v_e = 0.25, and τ_i = 0.45 s. Monte Carlo simulations (using Fig. 1A AIF as the β =1.0 reference) were used to estimate K^{trans}, v_e, and τ_i accuracy (mean) and precision (SD). 400 fittings were performed with random Gaussian noise (SNR = 10 at baseline, slightly better than the median baseline voxel SNR of 5.3 estimated from the prostate ROI slices of all subjects) added to the simulated time-course each time, and each fitting started with a different initial guess parameter value set. Mean and SD values of k_{ep} and k_{io} derived from the **3A** fittings are plotted in Figure 3B. Fig. 3A clearly shows that K^{trans} and v_e decrease proportionally (~ 30%) with the 30% β increase, while the τ_i change is negligibly small (< 3%), well below the standard deviation (~10%) associated with the data SNR. Defined as K^{trans}/v_e, k_{ep} is insensitive to β variation (Fig. 3B) as expected. Being the τ_i reciprocal, the rate constant k_{io} has a similar relative measurement error as τ_i. Except for having different numerical means, v_i and v_e have the same SD values because $v_i \equiv 1\text{-}v_e$. That is, error propagation for both v_e and v_i is exactly the same. Results of k_{io} (or τ_i) and k_{ep} being less sensitive to AIF scaling variations indicate that the values of these parameters are likely to be more consistent despite difficulties in accurate AIF determination in many experimental conditions. We use results from real prostate ROI data in the following figures to illustrate additional aspects also seen with simulations. This provides some validations of the simulation results and adds insights on actual data processing when AIF scaling uncertainty plays a factor in pharmacokinetic model parameters.

Figure 4A shows representative ROI K^{trans} variations associated with AIF scaling uncertainty, for malignant (black curves) and benign (gray curves) tissues. The individual AIF (= $\beta \cdot [CR_p]$) was used for fitting at each β value, mimicking AIF scaling uncertainty seen in experimental AIF derivation. Each ROI time-course was fitted with shutter-speed (solid curves) and tracer (dashed curves) analyses. The best fitted values returned from the 20 different initial parameter guess sets are plotted. The K^{trans} values are rather AIF scaling dependent, decreasing with increasing β. Similar findings are observed for the v_e parameter (Figure 4B). Both K^{trans} and v_e are the most commonly reported parameters in pharmacokinetic model fitting.

The simulated results in Fig. 2B indicate that k_{ep} appears to be independent of β scaling. This is confirmed by results from real prostate data (Figure 5). Averaged k_{ep} values of eight benign and five malignant ROIs (with standard errors), respectively, are plotted *versus* β values used in this study. For each signal-averaged ROI at each β step, 20 fittings with different initial guess each time were performed and the one with the smallest fitting error was then selected for that ROI. The results from shutter-speed analyses are plotted as square points and those from tracer analyses as circular points. The malignant ROIs are represented by black color vs. gray color for the benign group. Regardless of the analysis paradigm and tissue type, the k_{ep} within each analysis remains nearly constant at different β values, indicating k_{ep} is basically unaffected by AIF scaling uncertainty. The apparent malignant/benign discrimination [$k_{ep}(M) - k_{ep}(B)$] is increased with the shutter-speed paradigm (17,18) [double-headed vertical arrows in Fig. 5]. This trend is shown because when compared to their FXL counterparts, k_{ep} values determined by the FXR often increase for malignant cases and decrease for benign cases. Although this systematic behavior may not be covered by generic statistical tools, we report the Hedges' g effect size for malignant/benign separation by k_{ep} to provide a primitive numerical comparison. The computed Hedges' g values for k_{ep} mean differences are 1.15 (95% CI: 0.24, 2.07) and 0.82 (95% CI: −0.06, 1.70) for the FXL and FXR approaches, respectively. Future investigation with larger subject cohort is needed to address this issue more thoroughly.

Figure 6A shows a portion of an axial T_2-weighted image of a 66 year old subject with prostate malignancy. Figures 6B–6D show zoomed pharmacokinetic parametric maps (k_{io}, k_{ep}, and v_i, respectively) of the lesion area within the prostate, which is generally indicated by the yellow rectangle in Fig. 6a. The black borders in Figs. 6B–6D provide some contrast to the generally cold color of normal-appearing glandular tissue within the rectangular ROI encompassing the lesion. The parametric maps were obtained as the best results from 30 fittings with different initial guess sets. Elevated k_{io} values are seen in part of the lesion, possibly indicating increased cellular metabolic activity [7] associated with malignancy. Noticeably higher k_{ep} values reflecting increased vascular leakage are seen only in the anterior portion within the lesion ROI. Besides being on the "warm" portion of the color map (often brighter contrast), v_i is directly proportional to cell density.

In Figure 7, lesion ROI-averaged *in vivo* SSP-only k_{io} values are plotted against the independently-obtained *ex vivo* Gleason scores for the five malignant cases. Each voxel within each ROI was fitted 30 times with different initial guess values using both the shutter-speed paradigm and tracer paradigm. The best fitted results from each paradigm were

recorded. Then, the commonly used model selection approach, the Akaike information criterion (AIC), was used to determine which model better described the specific voxel time-course. In Figure 7, only those voxels favored by AIC for the shutter-speed paradigm were included in the averaging calculation [the tracer paradigm leaves k_{io} indeterminate]. Using the lesion ROI (indicated by the yellow rectangle) from Figure 6 as an example, k_{io} was averaged for 36 out of 38 voxels. The numbers of AIC-favored over the total ROI voxels for the remaining four malignant cases are: 23/56, 13/16, 8/11, and 20/28. A clear trend of increasing k_{io} with Gleason score (Spearman's correlation coefficient, $r = 0.91$; $p = 0.03$) is observed (the empirical blue dashed curve is intended only to guide the eye). The k_{io} error bars show standard errors for the analysis of each small lesion. The vertical error bars also reflect our unknown registration of MRI ROI and biopsy *locus*. That is, without clear knowledge of the latter, voxels from benign tissues can be accidentally included in the lesion ROIs. As CR extravasation is generally lower in non-cancerous tissue, k_{io} uncertainty increases because of decreased shutter speed [17], which results in larger error bar length compared to an ROI containing more malignant tissue. The horizontal error bars show calculated differences between clinical Gleason scores reported in another study, and the weighted mean Gleason scores given by an expert reviewer [24]. These bars partially illustrate the uncertainties in Gleason pattern reporting (*e.g.*, if no reported Gleason scores differ by two categorical points or larger, a 0.1 bar length then represents 10% of the cases having different Gleason scores). Other fitted parameter values from the same patient group were reported previously [6]. None of the fitted K^{trans} and v_e values from either paradigm showed a clear correlation with Gleason scores.

DISCUSSION

Accurate AIF quantification has been one of the primary challenges in quantitative pharmacokinetic analysis of DCE-MRI data. Many AIF derivation methods [5,6,11–16] require an AIF amplitude scaling in the process. Since the ground truth of the scaling factor is often unknown (for example, using muscle as a reference tissue for AIF scaling runs into the problem of varying pharmacokinetic properties of the muscle itself under different physiological conditions), this makes investigation of AIF scaling effects important. By explicitly including an AIF scaling factor (β) into the pharmacokinetic modeling, this work investigated the pharmacokinetic model parameter variations associated with AIF scaling uncertainty. Our results show that the k_{ep} and the SSP-specific k_{io} parameters are insensitive to AIF scaling. In a theoretical scenario where k_{ep} is truly time and [CR] independent, its insensitivity to $[CR_p]$ scaling can be directly predicted from Eq. (5). That is, k_{ep} insensitivity to AIF scaling is a direct result of the Kety-Schmitt pharmacokinetic rate law. This is the reason that insensitivity of k_{ep} to AIF scaling is observed for both the TP and the SSP approaches [Fig. 5]. On the other hand, the relative insensitivity of the SSP-specific k_{io} to AIF scaling is the result of multiple factors. First, k_{io} quantifies water exchange, which is a separate process independent of CR pharmacokinetics; second, the interstitial CR concentration, $[CR_o]$, generally experiences a more slow-varying temporal feature and reaches its maximum at a much later time when compared with $[CR_p]$ (*i.e.*, $[CR_o]$ is less sensitive to $[CR_p]$ first pass); third, k_{io} does not appear with $[CR_p]$ in the same term in a pharmacokinetic equation or within a $[CR_p]$ expression. One the other hand, a larger $[CR_p]$

helps reduce k_{io} uncertainty in CR-extravasating tissues by generating a larger $[CR_o]$ and thus a larger shutter speed [17].

Traditionally, the most common parameters extracted from quantitative DCE-MRI are K^{trans} and v_e. We found these parameters to be quite sensitive to the AIF scaling factor β over a range from 0.8 to 2.0 for both simulated (Fig. 3) and real prostate ROI data (Fig. 4). This may partially explain the no statistical difference findings [25,26] reported in literature when comparing pharmacokinetic parameters (K^{trans} and v_e) derived from population averaged AIFs vs. individually measured AIFs -- it is possible that the errors (specially AIF scaling uncertainty) in individually measured AIFs propagate to the fitted K^{trans} and v_e parameters and thus negatively impact their precisions as quantitative imaging biomarkers. Thus, when AIF amplitude uncertainty is high, the k_{io} and k_{ep} parameters are more robust DCE-MRI biomarkers for their relative AIF-scaling insensitivity. As long as the AIF time-course curve shape can be well captured, k_{io} and k_{ep} should be the more reproducible parameters than K^{trans} and v_e. With the recent discovery that k_{io} is a measure of on-going Na^+,K^+-ATPase turnover [7], the capability to quantify k_{io} using the SSP model potentially ushers DCE-MRI into the emerging field of high-resolution metabolic imaging [8], in addition to its well-known function of quantifying microvascular properties. The parameter k_{ep} could be a better measure of capillary CR permeation than K^{trans}. The parameter K^{trans} usually well-approximates the permeability coefficient capillary surface area product, $P_{CR}^{\dagger}$•S [8,27]. Thus, it can have a significant contribution from the voxel blood volume surface area. In addition, K^{trans} magnitude closely tracks the initial slope of the tissue enhancement time-course, a feature that describes similar characteristics of v_b•$[CR_p]$ (v_b is the blood volume). This is one reason that K^{trans} accuracy depends heavily on AIF. On the other hand, k_{ep} quantification depends more on the washout period of the tissue enhancement time-course. As shown in Figure 1B, a 10% k_{ep} change causes noticeable difference in only the washout phase. In this case, the K^{trans} difference is relatively small (~ 3 %) as the rising phase of the curves are nearly indistinguishable.

Figure 7 demonstrates the tumor grading potential of the new k_{io} biomarker for prostate cancer. Despite the k_{io} and Gleason score uncertainties shown by the error bars, the data show a strong correlation: k_{io} increases “hyperbolically” with Gleason scores above 5, the traditional malignancy threshold. The smooth curve drawn through the points serves only to guide the eye. Therefore, the k_{io} parameter may be a useful noninvasive imaging biomarker that can be potentially used to reduce the number of biopsies performed in current clinical practice.

It is worth noting that even though accurate AIF quantification remains challenging, especially during the CR first pass, an AIF scaling error of less than 30% can be managed from the washout phase, taking into account the total blood volume and CR elimination rate. It is important to point out that the precision in k_{io} quantification is better when CR extravasation is extensive (large K^{trans}) [7]. To insure k_{io} accuracy, we used 30 initial guess sets for each voxel during fitting, and limited our k_{io} report to voxels with AIC statistics favoring the shutter-speed paradigm.

The uncertainty in $[CR_o](t)$ quantification (because of AIF uncertainty) affects k_{io} and v_i accuracy, and the maximum $[CR_o]$ magnitude affects k_{io} precision [6,7]. It has recently been suggested it might be possible to determine k_{io} and v_i without the use of CR [28]. Though this is not yet established, it would preclude parametric errors due to AIF uncertainty. However, the K^{trans} and k_{ep} parameters are not accessible without the use of CR.

With faster imaging speed as a result of ever improving MRI scanner hardware and software, DCE-MRI data acquisition can achieve improved AIF temporal resolution and better tissue curve-shape quantifications. Still, intrinsic challenges, like the in-flow effect, associated with AIF quantification remain. These mostly affect the AIF magnitude. This study only examines the effects of this primary AIF scaling error. Implications of other AIF uncertainties on pharmacokinetic parameters will require separate investigation.

Using a mouse model, a recent study [29] utilizing X-ray fluorescence microscopy showed that gadodiamide (Omniscan) enters normal murine prostatic epithelia and lumens. Although it remains unclear whether CR also enters some tumor cells, this new finding may require to be accounted for with an additional compartment in prostate DCE-MRI pharmacokinetic modeling. It is unclear at this point whether the CR concentration differences between the prostatic epithelia, the lumens, and the EES are large enough to be separately resolved. Still, the new finding may partially explain the large v_e values reported in prostate DCE-MRI literature.

It is interesting to point out that for extracellular Gadolinium based CRs with appreciable extravasation, CR molecules will present in blood plasma and extravascular extracellular space (EES) after a bolus IV injection. The associated compartment-specific relaxivities for the EES and blood plasma are r_{1o} and r_{1p}, respectively. In most DCE-MRI studies it is generally assumed that r_{1o} and r_{1p} are numerically equal. However, there are some indirect evidences suggesting potential differences [30,31] between the two. Under the condition that r_{1o} and r_{1p} are both time-and [CR]-independent, the effect of unequal r_{1o} and r_{1p} on pharmacokinetic model parameter estimations is very similar to that of DCE data modeled under different AIF scaling factors, as was undertaken in this study. The similarity is shown in the APPENDIX.

The data studied here have also been used in two earlier reports [6, 5]. The former showed the shutter-speed K^{trans} and k_{ep} as well as the ΔK^{trans} [$\equiv K^{trans}$(FXR) - K^{trans}(FXL)] imaging biomarkers exhibit improved malignant/benign tissue discrimination [6]. The latter paper showed the CA extravasation magnitude effect on commonly modeled DCE parameter (K^{trans}, v_e, v_b τ_i, τ_b) precisions. Specifically, τ_i ($1/k_{io}$) uncertainty and the feasibility of τ_i ($1/k_{io}$) mapping of the entire normal prostate were demonstrated [5]. In this paper, after identifying k_{ep} and k_{io} as the AIF-scaling-insensitive DCE parameters, the potential for k_{io} (with its newly discovered metabolic activity nature) as a disease aggressiveness biomarker was shown: a k_{io} Gleason score correlation.

One limitation of this study is that we investigated the effect of only AIF scaling uncertainty on estimations of pharmacokinetic parameters. Other confounding factors, like variable T_2* effect during CR passage and in-flow effect, etc., can result in AIF curve shape variations,

which will cause different variations in the derived k_{ep} values. Future studies will be needed to address these issues. It is encouraging that a recent multi-center prostate DCE-MRI data analysis study showed that the variations of the k_{ep} parameter were substantially smaller than those of the K^{trans} parameter when they were derived from AIFs quantified with different methods, leading to both AIF curve-shape and amplitude differences [32].

CONCLUSIONS

AIF quantification remains a major challenge for DCE-MRI pharmacokinetics. Several AIF derivation approaches require AIF magnitude scaling, which generally suffers from the lack of ground truth knowledge. This simulation work demonstrates that the k_{ep} and the Shutter-Speed Paradigm specific k_{io} ($1/\tau_i$) parameters are nearly insensitive to AIF scaling. This supports the notion that both the k_{ep} and k_{io} parameters are more robust DCE-MRI biomarkers.

Acknowledgments

This work was supported in part by the Medical Research Foundation of Oregon and National Institute of Health grants: RO1-EB00422, U01-CA154602, R44 CA180425.

Abbreviations

AIF	arterial input function
AIF scaling factor	β
CR	contrast reagent
$[CR_p]$	contrast reagent concentration in blood plasma
$[CR_o]$	contrast reagent concentration in the extravascular, extracellular space
$[CR_t]$	contrast reagent concentration in tissue
DCE-MRI	dynamic contrast-enhanced magnetic resonance imaging
FOV	field of view
FXL	fast-exchange-limit
FXR	fast-exchange-regime
h_v	microvascular hematocrit
K^{trans}	rate constant for plasma/interstitium contrast agent transfer
k_{ep}	$= K^{trans}/v_e$, rate constant for contrast reagent intravasation
k_{io}	$= 1/\tau_i$, unidirectional equilibrium cellular water efflux rate constant
PD	proton density

r_1	longitudinal contrast reagent relaxivity
r_{1o}	longitudinal relaxivity for CR in the extravascular, extracellular space
r_{1p}	longitudinal relaxivity for CR in the blood plasma space
R_{1b}	= $1/T_{1b}$, blood longitudinal relaxation rate constant for blood ^1H_2O
R_{1t}	= $1/T_{1t}$, tissue longitudinal relaxation rate constant for tissue ^1H_2O
ROI	region of interest
ρ	cell number density [number of cells/unit volume]
SD	standard deviation
SNR	signal-to-noise ratio
SSP	Shutter-Speed Paradigm
SXR	slow-exchange-regime
τ_i	mean intracellular water lifetime
T_1^{-1}	= ($\|R_{1o} - R_{1i}\|$), the NMR R_1"shutter-speed", [$\equiv \kappa_1$]
TP	Tracer Paradigm (Tofts model)
v_e	extravascular, extracellular volume fraction; the EES
v_i	intracellular volume fraction (= 1- v_e, when ignoring blood volume fraction)

References

1. Li X, Huang W, Morris EA, Tudorica LA, Seshan VE, Rooney WD, Tagge I, Wang Y, Xu J, Springer CS Jr. Dynamic NMR effects in breast cancer dynamic-contrast-enhanced MRI. Proc Natl Acad Sci U S A. 2008; 105:17937–17942. [PubMed: 19008355]
2. Huang W, Li X, Morris EA, Tudorica LA, Seshan VE, Rooney WD, Tagge I, Wang Y, Xu J, Springer CS. The magnetic resonance shutter speed discriminates vascular properties of malignant and benign breast tumors in vivo. Proc Natl Acad Sci U S A. 2008; 105:17943–17948. [PubMed: 19004780]
3. Li X, Rooney WD, Varallyay CG, Gahramanov S, Muldoon LL, Goodman JA, Tagge IJ, Selzer AH, Pike MM, Neuwelt EA, Springer CS Jr. Dynamic-contrast-enhanced-MRI with extravasating contrast reagent: rat cerebral glioma blood volume determination. J Magn Reson. 2010; 206:190–199. [PubMed: 20674422]
4. Huang W, Tudorica LA, Li X, Thakur SB, Chen Y, Morris EA, Tagge IJ, Korenblit ME, Rooney WD, Koutcher JA, Springer CS Jr. Discrimination of benign and malignant breast lesions by using shutter-speed dynamic contrast-enhanced MR imaging. Radiology. 2011; 261:394–403. [PubMed: 21828189]

5. Li X, Priest RA, Woodward WJ, Siddiqui F, Beer TM, Garzotto MG, Rooney WD, Springer CS Jr. Cell membrane water exchange effects in prostate DCE-MRI. J Magn Reson. 2012; 218:77–85. [PubMed: 22578558]
6. Li X, Priest RA, Woodward WJ, Tagge IJ, Siddiqui F, Huang W, Rooney WD, Beer TM, Garzotto MG, Springer CS Jr. Feasibility of shutter-speed DCE-MRI for improved prostate cancer detection. Magn Reson Med. 2013; 69:171–178. [PubMed: 22457233]
7. Springer CS Jr, Li X, Tudorica LA, Oh KY, Roy N, Chui SY, Naik AM, Holtorf ML, Afzal A, Rooney WD, Huang W. Intratumor mapping of intracellular water lifetime: metabolic images of breast cancer? NMR Biomed. 2014; 27:760–773. [PubMed: 24798066]
8. Rooney WD, Li X, Sammi MK, Bourdette DN, Neuwelt EA, Springer CS Jr. Mapping human brain capillary water lifetime: high-resolution metabolic neuroimaging. NMR Biomed. 2015; 28:607–623. [PubMed: 25914365]
9. Preston E, Foster DO. Diffusion into rat brain of contrast and shift reagents for magnetic resonance imaging and spectroscopy. NMR Biomed. 1993; 6:339–344. [PubMed: 8268067]
10. Nagaraja TN, Ewing JR, Karki K, Jacobs PE, Divine GW, Fenstermacher JD, Patlak CS, Knight RA. MRI and quantitative autoradiographic studies following bolus injections of unlabeled and (14)C-labeled gadolinium-diethylenetriaminepentaacetic acid in a rat model of stroke yield similar distribution volumes and blood-to-brain influx rate constants. NMR Biomed. 2011; 24:547–558. [PubMed: 21674656]
11. Kovar DA, Lewis M, Karczmar GS. A new method for imaging perfusion and contrast extraction fraction: input functions derived from reference tissues. J Magn Reson Imaging. 1998; 8:1126–1134. [PubMed: 9786152]
12. Yang C, Karczmar GS, Medved M, Stadler WM. Estimating the arterial input function using two reference tissues in dynamic contrast-enhanced MRI studies: fundamental concepts and simulations. Magn Reson Med. 2004; 52:1110–1117. [PubMed: 15508148]
13. Yang C, Karczmar GS, Medved M, Stadler WM. Multiple reference tissue method for contrast agent arterial input function estimation. Magn Reson Med. 2007; 58:1266–1275. [PubMed: 17969061]
14. Schabel MC, Fluckiger JU, DiBella EV. A model-constrained Monte Carlo method for blind arterial input function estimation in dynamic contrast-enhanced MRI: I. Simulations. Phys Med Biol. 2010; 55:4783–4806. [PubMed: 20679691]
15. Fluckiger JU, Schabel MC, DiBella EV. Toward local arterial input functions in dynamic contrast-enhanced MRI. J Magn Reson Imaging. 2010; 32:924–934. [PubMed: 20882623]
16. Kratochvila J, Jirik R, Bartos M, Standara M, Starcuk Z Jr, Taxt T. Distributed capillary adiabatic tissue homogeneity model in parametric multi-channel blind AIF estimation using DCE-MRI. Magn Reson Med. 2016; 75:1355–1365. [PubMed: 25865576]
17. Li X, Rooney WD, Springer CS Jr. A unified magnetic resonance imaging pharmacokinetic theory: intravascular and extracellular contrast reagents. Magn Reson Med. 2005; 54:1351–1359. [Erratum: Magn. Reson. Med. 55 (2006) 1217.]. [PubMed: 16247739]
18. Yankeelov TE, Rooney WD, Li X, Springer CS Jr. Variation of the relaxographic “shutter-speed” for transcytolemmal water exchange affects the CR bolus-tracking curve shape. Magn Reson Med. 2003; 50:1151–1169. [PubMed: 14648563]
19. Rohrer M, Bauer H, Mintorovitch J, Requardt M, Weinmann HJ. Comparison of magnetic properties of MRI contrast media solutions at different magnetic field strengths. Invest Radiol. 2005; 40:715–724. [PubMed: 16230904]
20. Landis CS, Li X, Telang FW, Molina PE, Palyka I, Vetek G, Springer CS Jr. Equilibrium transcytolemmal water-exchange kinetics in skeletal muscle in vivo. Magn Reson Med. 1999; 42:467–478. [PubMed: 10467291]
21. Wilson GJ, Woods M, Springer CS Jr, Bastawrous S, Bhargava P, Maki JH. Human whole-blood (1)H2O longitudinal relaxation with normal and high-relaxivity contrast reagents: influence of trans-cell-membrane water exchange. Magn Reson Med. 2014; 72:1746–1754. [PubMed: 24357240]
22. Tofts PS, Brix G, Buckley DL, Evelhoch JL, Henderson E, Knopp MV, Larsson HB, Lee TY, Mayr NA, Parker GJ, Port RE, Taylor J, Weisskoff RM. Estimating kinetic parameters from dynamic

contrast-enhanced T(1)-weighted MRI of a diffusable tracer: standardized quantities and symbols. J Magn Reson Imaging. 1999; 10:223–232. [PubMed: 10508281]

23. Bevington, PR. Data Reduction and Error Analysis for the Physical Sciences. McGraw-Hill; New York: 1969.
24. Goodman M, Ward KC, Osunkoya AO, Datta MW, Luthringer D, Young AN, Marks K, Cohen V, Kennedy JC, Haber MJ, Amin MB. Frequency and determinants of disagreement and error in gleason scores: a population-based study of prostate cancer. Prostate. 2012; 72:1389–1398. [PubMed: 22228120]
25. Meng R, Chang SD, Jones EC, Goldenberg SL, Kozlowski P. Comparison between population average and experimentally measured arterial input function in predicting biopsy results in prostate cancer. Acad Radiol. 2010; 17:520–525. [PubMed: 20074982]
26. Shukla-Dave A, Lee N, Stambuk H, Wang Y, Huang W, Thaler HT, Patel SG, Shah JP, Koutcher JA. Average arterial input function for quantitative dynamic contrast enhanced magnetic resonance imaging of neck nodal metastases. BMC Med Phys. 2009; 9:4. [PubMed: 19351382]
27. Li X, Springer CS Jr, Jerosch-Herold M. First-pass dynamic contrast-enhanced MRI with extravasating contrast reagent: evidence for human myocardial capillary recruitment in adenosine-induced hyperemia. NMR Biomed. 2009; 22:148–157. [PubMed: 18727151]
28. Hamilton JI, Deshmane A, Hougen S, Griswold M, Seiberlich N. Magnetic Resonance Fingerprinting with Chemical Exchange (MRF-X) for Quantification of Subvoxel T1, T2, Volume Fraction, and Exchange Rate. Proc Intl Soc Mag Reson Med. 2015; 23:329.
29. Mustafi D, Gleber SC, Ward J, Dougherty U, Zamora M, Markiewicz E, Binder DC, Antic T, Vogt S, Karczmar GS, Oto A. IV Administered Gadodiamide Enters the Lumen of the Prostatic Glands: X-Ray Fluorescence Microscopy Examination of a Mouse Model. AJR Am J Roentgenol. 2015; 205:W313–9. [PubMed: 26295667]
30. Stanisz GJ, Henkelman RM. Gd-DTPA relaxivity depends on macromolecular content. Magn Reson Med. 2000; 44:665–667. [PubMed: 11064398]
31. Wang Y, Spiller M, Caravan P. Evidence for weak protein binding of commercial extracellular gadolinium contrast agents. Magn Reson Med. 2010; 63:609–616. [PubMed: 20146229]
32. Huang W, Chen Y, Fedorov A, Li X, Jajamovich GH, Malyarenko DI, Aryal MP, LaViolette PS, Oborski MJ, O'Sullivan F, Abramson RG, Jafari-Khouzani K, Afzal A, Tudorica A, Moloney B, Gupta SN, Besa C, Kalpathy-Cramer J, Mountz JM, Laymon CM, Muzi M, Kinahan PE, Schmainda K, Cao Y, Chenevert TL, Taouli B, Yankeelov TE, Fennessy F, Li X. The Impact of Arterial Input Function Determination Variations on Prostate Dynamic Contrast-Enhanced Magnetic Resonance Imaging Pharmacokinetic Modeling: A Multicenter Data Analysis Challenge. Tomography. 2016; 2:56–66. [PubMed: 27200418]

APPENDIX

The relaxivity of a contrast reagent (CR) is defined as the slope of the R_1 and [CR] equation as expressed in Eq. (1a),

$$R_1 = r_1 \cdot [CR] + R_{10} \quad (1a)$$

where r_1 is the relaxivity in unit of ($mM^{-1}s^{-1}$).

The r_1 values are specific to the compartments occupied by CR molecules. In DCE-MRI, low molecular weight Gadolinium based CR can present in blood plasma and the extravascular, extracellular space (EES).

Eq. (3) can be used to convert measured blood R_1 time-course to that of blood plasma CR concentration time-course, [CR_p].

For the FXR and the FXL models, the relationships of tissue R_1 and the EES CR concentration, $[CR_o]$, is given by Eq. (1) and Eq. (5), respectively.

Because r_1 always appears in the form of r_1•[CR] product in a relaxivity expression, the r_{1o}•$[CR_o]$ term which quantifies EES R_1 change can be expanded to:

$$r_{1o}[CR_o](t)=\frac{r_{1o}}{r_{1p}}\cdot\left(\frac{K^{trans}}{v_e}\right)\cdot\frac{1}{(1-h_v)}\cdot\int_0^T(R_{1b}(t)-R_{1b}(0))\cdot\exp\left(-\frac{K^{trans}}{v_e}\cdot(T-t)\right)\cdot dt \quad (2a)$$

where r_{1o} is the longitudinal CR relaxivity for the EES, and r_{1p} is the longitudinal CR relaxivity for blood plasma. All other parameters are defined in MATERIALS and METHODS section.

It is common practice in DCE-MRI pharmacokinetic modeling to assume that $r_{1o} = r_{1p.}$ However, there is some evidence indicating unequal r_{1o} and r_{1p} values [30,31].

When both r_{1o} and r_{1p} are [CR]- and time-independent, the r_{1o}/r_{1p} ratio can be moved to either side of Eq. (2a). That is, $r_{1o}/r_{1p} \neq 1.0$ has a similar effect as that of employing an AIF scaling factor (β) in pharmacokinetic modeling. Here, the AIF is assumed to be well-characterized and the r_{1o}/r_{1p} ratio depends on the compartments the CR molecules occupy. When the r_{1o}/r_{1p} ratio is unknown or there is strong evidence indicating that $r_{1o}/r_{1p} \neq 1.0$, then results from this work show that k_{ep} can be the parameter preferred over K^{trans} for characterizing microvasculature. This is because of its insensitivity to AIF scaling uncertainties.

Highlights

- In DCE-MRI pharmacokinetic modeling, arterial input function (AIF) scaling is often needed for AIF derivation.
- Contrast reagent transfer constant (K^{trans}) and extravascular, extracellular volume fraction (v_e) model parameters are affected by AIF-scaling.
- The contrast reagent intravasation rate constant (k_{ep}) is insensitive to AIF-scaling error.
- The unidirectional rate constant for equilibrium cellular water efflux (k_{io}) is insensitive to AIF-scaling error.

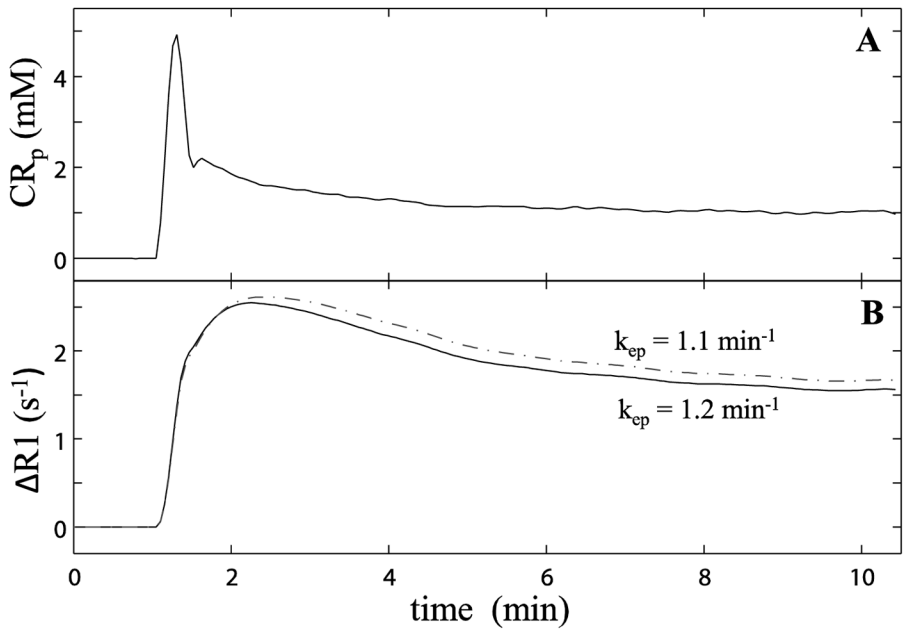

Figure 1.

Figure 1A plots the averaged blood plasma concentration ($[CR_p]$) time-course derived from five individually determined arterial input functions [AIFs]. Under the condition of β =1.3 (i.e., 130% the 1A AIF amplitude), the **1B** solid curve plots the $\Delta R_1(t)$ time-course calculated with K^{trans} = 0.36 min^{-1}, v_e = 0.3 (k_{ep} =1.2 min^{-1}), τ_i = 0.6. The dashed curve traces $\Delta R_1(t)$ with a different parameter set: K^{trans} = 0.35 min^{-1}, v_e = 0.32 (k_{ep} =1.1 min^{-1}), τ_i = 0.6 s.

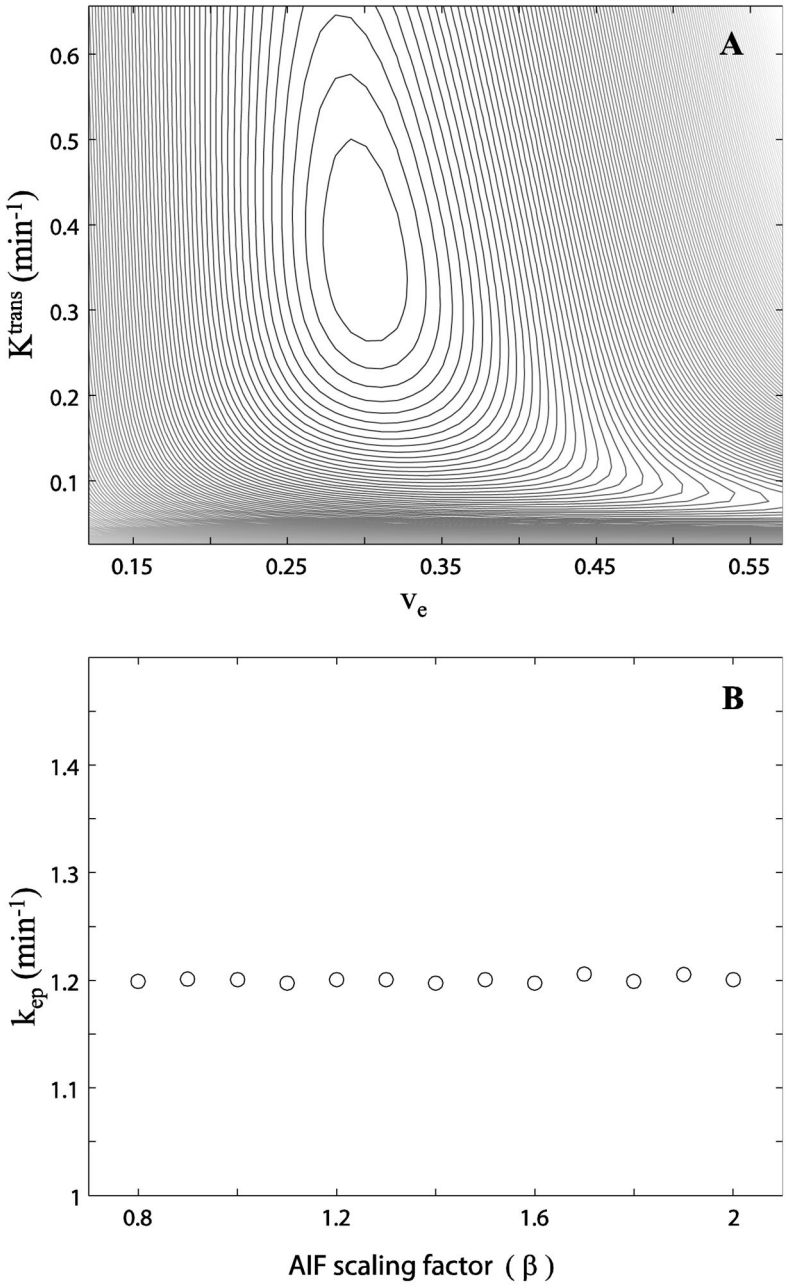

Figure 2.

Figure 2A shows a K^{trans} vs. v_e error surface. The contour plot shows the chi square statistic, $\chi^2 = \Sigma[S_{ref}(t) - S_{grid}(t)]^2$, for simulated DCE-MRI time-courses from parameters equal to the K^{trans},v_e coordinates. The χ^2 value decreases as the contour lines move towards the center of the closed loops. **B** shows the best k_{ep} ($\equiv K^{trans}/v_e$) values determined at different β values. A near constant k_{ep} is observed within the entire β range tested.

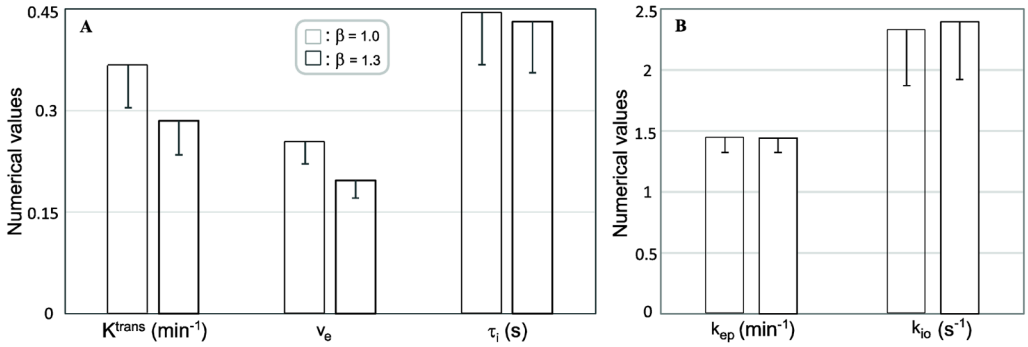

Figure 3.

Figure 3A depicts the K^{trans}, v_e, and τ_i changes associated with a 30% change in β. Monte Carlo simulations were used to estimate K^{trans}, v_e, and τ_i accuracy (mean) and precision (SD) changes resulting from a 30% β increase. It is seen that K^{trans} and v_e change proportionately (~ 30%) with β, while the τ_i change is negligibly small (< 3%), well below the standard deviation (>10%) associated with the data SNR. **3B** shows the similar plots for k_{ep} and k_{io}. Defined as K^{trans}/v_e, k_{ep} is insensitive to β variation as discussed in the text. Being the τ_i reciprocal, the rate constant k_{io} has the same relative error as that of τ_i.

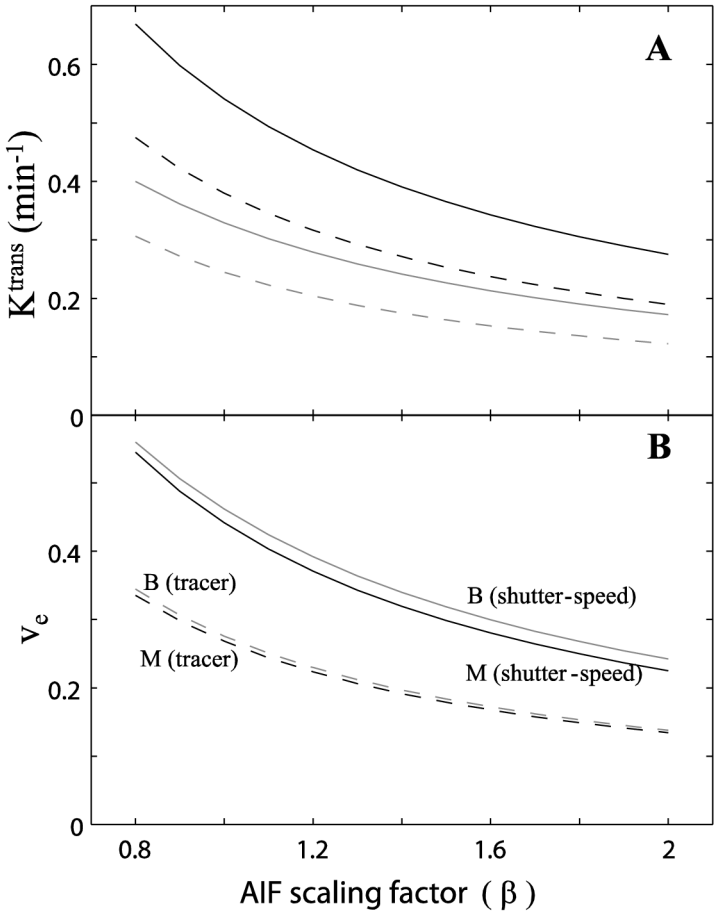

Figure 4.

Figure 4A shows representative K^{trans} changes for malignant (black curves) and benign (gray curves) tissues with increasing β. Each ROI data set was fitted with models from the shutter-speed (solid curves) and tracer (dashed curves) paradigms. The best fitted values from 20 different initial guesses are plotted. The K^{trans} values decrease with β increase. **4B** shows the same trends for v_e.

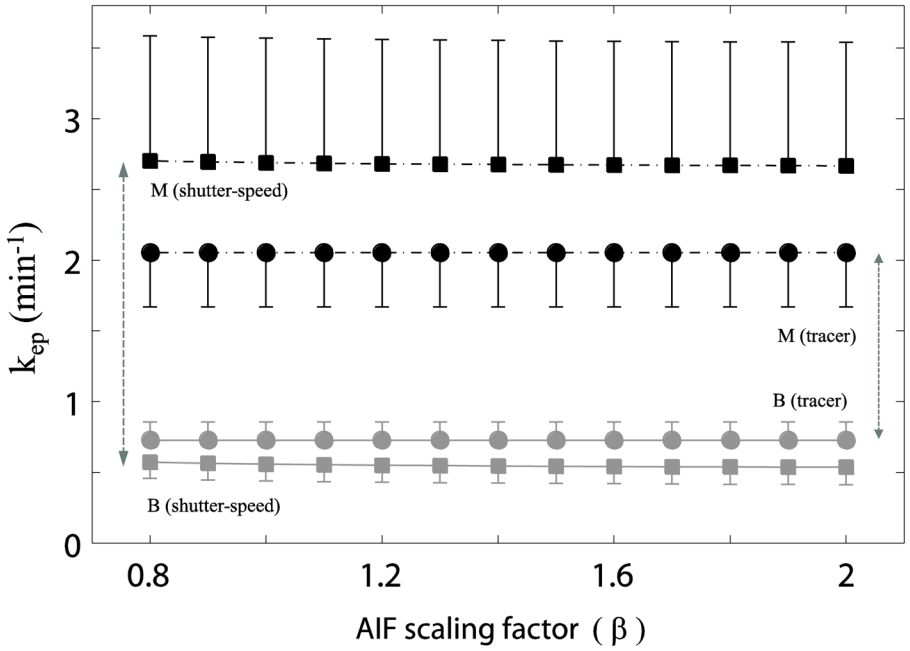

Figure 5.

Figure 5 plots the β-dependence of the mean k_{ep} values for the five malignant (black) and eight benign (gray) cases. The shutter-speed k_{ep} values have square symbols while the tracer values have circle symbols. Regardless of the pharmacokinetic paradigm and tissue characteristics, the k_{ep} value for each model remains constant, indicating k_{ep} is insensitive to AIF scaling.

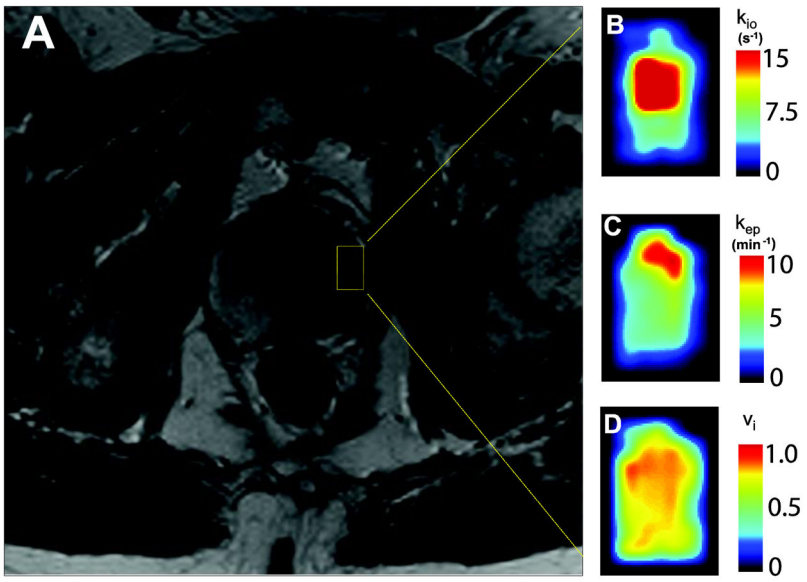

Figure 6.

Figure 6A shows a portion of an axial pelvic T_2-weighted image of a 66 year old subject with left prostate malignancy (anterior up). **Figures 6B–6D** show zoomed parametric maps of a tumor-encompassing ROI in the left prostate indicated by the 6A yellow rectangle. Figure 6B is the k_{io} map, which displays metabolic activity. Significantly elevated k_{io} is clearly visible in the anterior half of the ROI. Figure 6C shows increased k_{ep} in only the most anterior portion of the ROI. The k_{ep} parameter measures capillary CR permeability. Figure 6D shows v_i slightly elevated in the anterior half of the ROI. This most likely represents increased cell density. Black borders are added in 6B–6D to provide contrast with the elevated parametric color maps.

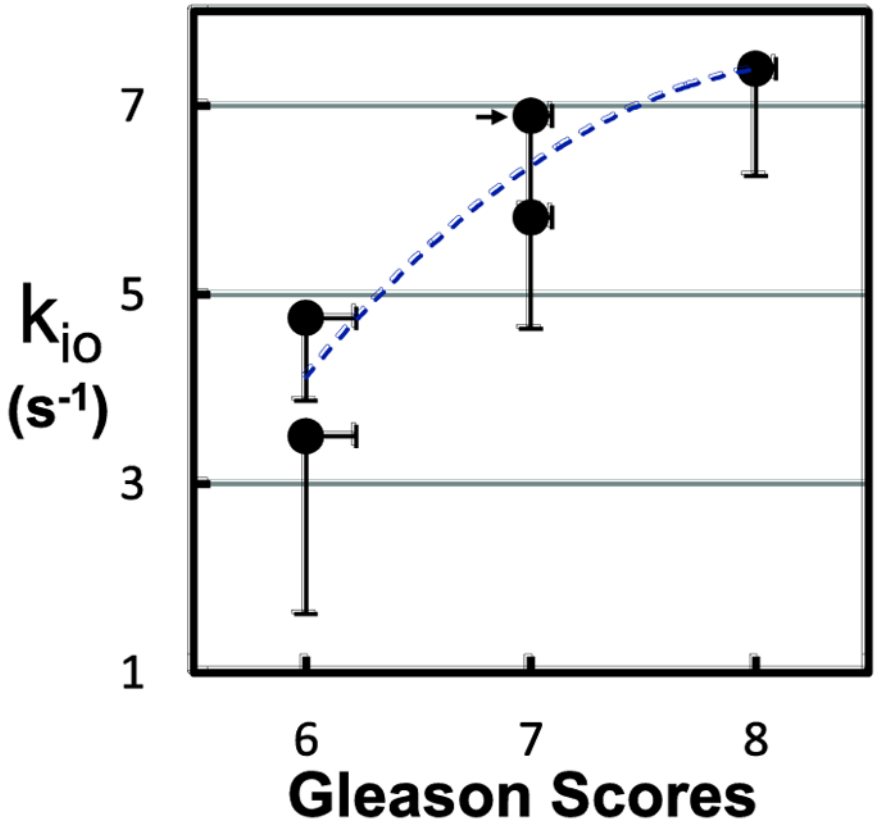

Figure 7.

Figure 7 plots lesion ROI-averaged *in vivo* k_{io} values against independently obtained *ex vivo* Gleason scores for the five malignant cases. A clear trend of increasing k_{io} with Gleason score (Spearman's correlation coefficient, r = 0.91; p = 0.03) is observed (the empirical blue dashed curve is intended only to guide the eye). The error bars show k_{io} standard errors and estimated Gleason score errors (see text).